






Charge density wave-templated spin cycloid in topological semimetal $\text{NdSb}_x\text{Te}_{2-x-\delta}$ Tyger H. Salters ¹, Fabio Orlandi ², Tanya Berry ¹, Jason F. Khoury ¹, Ethan Whittaker,¹
Pascal Manuel,² and Leslie M. Schoop ^{1,*}¹*Department of Chemistry, Princeton University, Princeton, New Jersey 08544, USA*²*ISIS Neutron Pulsed Facility, Science and Technology Facilities Council, Rutherford Appleton Laboratory, Oxford OX11 0QX, United Kingdom*

(Received 21 December 2022; revised 3 March 2023; accepted 31 March 2023; published 26 April 2023)

Magnetic topological semimetals present open questions regarding the interplay of crystal symmetry, magnetism, band topology, and electron correlations. $\text{LnSb}_x\text{Te}_{2-x-\delta}$ (Ln denotes Lanthanide) is a family of square-net-derived topological semimetals that allows compositional control of band filling, and access to different topological states via an evolving charge density wave (CDW) distortion. Previously studied Gd and Ce members containing a CDW have shown complex magnetic phase diagrams, which implied that spins localized on Ln interact with the CDW, but to this date no magnetic structures have been solved within the CDW regime of this family of compounds. Here, we report on the interplay of the CDW with magnetism in $\text{NdSb}_x\text{Te}_{2-x-\delta}$ by comparing the undistorted square net member $\text{NdSb}_{0.94}\text{Te}_{0.92}$ with the CDW-distorted phase $\text{NdSb}_{0.48}\text{Te}_{1.37}$, via single-crystal x-ray diffraction, magnetometry, heat capacity, and neutron powder diffraction. $\text{NdSb}_{0.94}\text{Te}_{0.92}$ is a collinear antiferromagnet with $T_N \sim 2.7$ K, where spins align antiparallel to each other, but parallel to the square net of the nuclear structure. $\text{NdSb}_{0.48}\text{Te}_{1.37}$ exhibits a nearly fivefold-modulated CDW ($q_{\text{CDW}} = 0.18$), isostructural to other $\text{LnSb}_x\text{Te}_{2-x-\delta}$ at similar x . $\text{NdSb}_{0.48}\text{Te}_{1.37}$ displays more complex magnetism with $T_N = 2.3$ K, additional metamagnetic transitions, and an elliptical cycloid magnetic structure with $q_{\text{mag}} = -0.41b^*$. The magnitudes of q_{CDW} and q_{mag} exhibit an integer relationship, $1 + 2q_{\text{mag}} = q_{\text{CDW}}$, implying a coupling between the CDW and magnetic structure. Given that the CDW is localized within the nonmagnetic distorted square net, we propose that conduction electrons “template” the spin modulation via the Ruderman-Kittel-Kasuya-Yosida interaction.

DOI: [10.1103/PhysRevMaterials.7.044203](https://doi.org/10.1103/PhysRevMaterials.7.044203)

I. INTRODUCTION

In the search for new topological matter, materials with a square-net structural motif have been heavily studied as a popular platform to host topological electronic states [1–8]. The p_x and p_y orbitals that contribute much of the bonding in the square-net yield band structures with multiple topological band crossings, and thus the materials have been found to host Dirac, Weyl, and nodal line topological semimetals (TSMs), as well as topological insulators [9–11]. From a chemical standpoint, the bonding within the square net can be described as “hypervalent,” which means that it is delocalized over the square net, as the electrons occupy an exactly half-filled p_x/p_y band. Deviation from a half-filled electron count will disturb this type of bonding, causing electron localization that is accommodated by distortions of the net [12]. Such a deviation is reflected in the band structure by the appearance of nesting at the Fermi surface, wherein pockets coincide by translation of some wave vector \mathbf{q} [13]. Such an instability can be alleviated by formation of a charge density wave (CDW), in which bond localization, also influenced by electron-phonon coupling, leads to a periodic distortion of the structure with a modulation wave vector reflecting the nesting vector \mathbf{q} [14].

The canonical nodal line semimetal ZrSiS , as well as several isostructural relatives, contains a nodal line at the Fermi level and a nonsymmorphic Dirac node above E_F [11]. Members of the family crystallize in the tetragonal $P4/nmm$ space group, in which, if using ZrSiS as an example, the Si square net lies in the ab plane. The square net is sandwiched by layers of Zr and S along the c axis, in a puckered rocksalt layer between each square net. One isostructural subgroup of the ZrSiS family, LnSbTe (Ln denotes Lanthanide), affords chemical tuning of E_F by substitution of Te into the Sb square net [15], allowing access to the nonsymmorphic Dirac node; such solid solutions are largely overlooked by popular databases used to predict TSMs due to the limits of the computational methods which they are built upon [16–19]. Magnetic rare-earth ions also make the LnSbTe family attractive to study the interplay of topological states with magnetism. This allows for opportunities to observe new topological states through the breaking of time-reversal symmetry, leveraging magnetic order as another tunable parameter to control electronic structure and access multiple topologically distinct phases. $\text{LnSb}_x\text{Te}_{2-x-\delta}$ (δ indicating vacancy concentration in the square net) materials also exhibit charge density waves (CDWs), which are coupled with structural distortions in the square net that evolve continuously with Sb/Te composition, and are a result of changes in band filling within the square net [20–22]. We have recently reported that the

*lschoop@princeton.edu

CDW is responsible for the gapping of topologically trivial states in $\text{GdSb}_{0.46}\text{Te}_{1.48}$, yielding an ideal nonsymmorphic Dirac semimetal band structure free of all other states about E_F , separated by hundreds of meV [15]. Depending of the doping level, the CDW can have one or multiple q -vectors that describe the structure modulation. The single q -vector region usually lies in the intermediate doping range. Here, the q -vector is in-plane and agrees with a nesting vector that connects the two sheets of the diamond-shaped Fermi surface that is typical of such square-net materials [15,20]. $\text{GdSb}_x\text{Te}_{2-x-\delta}$ also displays highly complex magnetism in which magnetic phase diagrams evolve with the compositionally driven CDW [23]. In-plane magnetic anisotropy has been reported in mechanically detwinned $\text{GdSb}_{0.46}\text{Te}_{1.48}$ crystals, indicating that the unidirectional CDW distortion yields especially complex H-T magnetic phase diagrams along the direction of the distortion. Notably, magneto-entropic analysis of this composition also suggests the signature of an antiferromagnetic skyrmion phase at low applied field [23]. Across all distorted phases, the CDW does not significantly distort the puckered magnetic $Ln\text{Te}$ layers in the parent structure. However, the evolving distortion and composition of the nonmagnetic (Sb,Te) square net is suggested to influence couplings through Ruderman-Kittel-Kasuya-Yosida (RKKY) interaction. RKKY interactions are sensitive to the also-evolving density of states, yielding a Sb-concentration-dependent magnetic phase diagram.

The highly neutron-absorbing nature of Gd complicates the feasibility of determining the magnetic structures of $\text{GdSb}_x\text{Te}_{2-x-\delta}$ with neutron diffraction. In an effort to study evolving magnetism and topology with neutron-friendly analogs, we have previously synthesized isostructural $\text{CeSb}_x\text{Te}_{2-x-\delta}$ [22]. The stoichiometric parent compound, CeSbTe , is capable of switching between Dirac and Weyl semimetal states by changing the strength of an applied magnetic field [24]. Single-crystal x-ray diffraction (SCXRD) has shown that CDWs are continuously tunable in $\text{CeSb}_x\text{Te}_{2-x-\delta}$ and exhibit modulated structures consistent with $\text{GdSb}_x\text{Te}_{2-x-\delta}$ at similar Sb compositions. Distortions and calculations on $\text{CeSb}_{0.51}\text{Te}_{1.40}$ suggest that the approach of driving CDWs to discover “clean” TSMs can be extended to several members of the $Ln\text{Sb}_x\text{Te}_{2-x-\delta}$ family [22]. In the single- q CDW region of the phase diagram, the magnetism of $\text{CeSb}_x\text{Te}_{2-x-\delta}$ does not exhibit the same complexity, but it does yield a composition and distortion-dependent magnetic phase diagram. Spins align out-of-plane in $\text{CeSb}_x\text{Te}_{2-x-\delta}$, perpendicular to the square net, which is consistent with neutron diffraction studies of the parent compound, CeSbTe [24], and divergent from $\text{GdSb}_x\text{Te}_{2-x-\delta}$, which exhibits an in-plane easy axis. Thus, in the Ce system, the spins do not align with the CDW q -vector, at least in the single q -vector region, which might be the cause of its less complex magnetism. We now direct our efforts to a different neutron-friendly analog, $\text{NdSb}_x\text{Te}_{2-x-\delta}$, where spins are oriented in-plane, similarly to $\text{GdSb}_x\text{Te}_{2-x-\delta}$.

NdSbTe has been reported to exhibit metamagnetic transitions and field-dependent transport, implying an interaction of magnetism with electronic structure [25]. Herein we report the magnetism and magnetic structures of $\text{NdSb}_{0.91}\text{Te}_{0.89}$ and $\text{NdSb}_{0.48}\text{Te}_{1.37}$, two members of $\text{NdSb}_x\text{Te}_{2-x-\delta}$, which we

TABLE I. Easy-axis and neutron absorptivity in $Ln\text{Sb}_x\text{Te}_{2-x-\delta}$.

$(Ln \text{ in } Ln\text{Sb}_x\text{Te}_{2-x-\delta})$	Spin alignment	Neutron absorption cross-section (barn) [26]
Gd	\rightarrow ($\parallel ab$) [23]	49700
Ce	\uparrow ($\perp ab$) [22]	0.63
Nd	\rightarrow ($\parallel ab$) ^{this work}	50.5

studied by magnetometry, single-crystal x-ray diffraction, and neutron powder diffraction. $\text{NdSb}_{0.91}\text{Te}_{0.89}$ is found to have a crystal structure consistent with other tetragonal $Ln\text{Sb}_x\text{Te}_{2-x-\delta}$ phases, and it exhibits a collinear magnetic structure in which spins align within the ab plane (see Table I). $\text{NdSb}_{0.48}\text{Te}_{1.37}$ is nearly isostructural to $\text{GdSb}_{0.46}\text{Te}_{1.48}$ with a single- q CDW modulation, and it displays a complex elliptical cycloid magnetic structure. The magnitude of the magnetic propagation vector q_{mag} is found to have an integer relationship with that of q_{CDW} , $1 + 2q_{\text{mag}} = q_{\text{CDW}}$, which implies the interaction of conduction electrons from the distorted square net with the unpaired electrons in Nd that led to magnetism, which are considered to sit at energy levels far below the Fermi energy. This is the first magnetic structure solved for a CDW $Ln\text{Sb}_x\text{Te}_{2-x-\delta}$ phase, and it may provide insight into the interaction between magnetism and topological bands in these “ideal” TSMs.

II. EXPERIMENT

A. Synthesis of $\text{NdSb}_{0.91}\text{Te}_{0.89}$ and $\text{NdSb}_{0.48}\text{Te}_{1.37}$

Single crystals of $\text{NdSb}_{0.91}\text{Te}_{0.89}$ and $\text{NdSb}_{0.48}\text{Te}_{1.37}$ were prepared using a chemical vapor transport (CVT) method. Prior to CVT growth, precursor powders with nominal compositions of $\text{NdSb}_{0.5}\text{Te}_{1.5}$ and NdSbTe were prepared from Nd pieces (Sigma Aldrich, 99.9%), Sb shot (Alfa Aesar, 99.999%), and Te pieces, which were purified in-house after purchase from a commercial source (Sigma Aldrich, 99.999%). The elements were loaded into a 12 mm fused quartz tube and flame sealed under vacuum with an Ar backfill at approximately 60 mTorr, heated to 1000 °C over 12 h, held for 2 days, and cooled over 12 h in a box furnace. The resulting powders were ground and loaded into a 16 mm tube with 120 mg I_2 as a vapor transport agent, sealed under vacuum resulting in tubes of 6–8 cm in length. CVT growth was carried out by placing the tubes in a single zone tube furnace, with the powder sides placed in the middle of the furnace to create a thermal gradient at the sink side. The tubes were heated to 1000 °C over 12 h, held for 7 days, and cooled over 12 h, resulting in crystals formed at the sink end.

The elemental composition and approximate stoichiometry of the samples were confirmed via scanning electron microscopy (SEM)/energy-dispersive spectroscopy (EDS). An external standard of NdTe_3 was used to calibrate the measured Nd:Te ratio in the presence of Te vacancy. Multiple spectra were collected and averaged across multiple crystals to determine accurate compositions and confirm composition uniformity within a growth batch. In attempted preparation of NdSbTe , Sb loss was frequently observed during CVT growth, confirmed by composition analysis.

Powder phase samples for neutron diffraction were prepared from the elements using a vapor-assisted technique. Samples were sealed in quartz tubes with I_2 identical to the previously described procedure. The tubes were heated in a box furnace to 950°C over 12 h, held for 7 days, and cooled over 12 h, yielding highly crystalline powders. Single crystals of $\text{NdSb}_{0.48}\text{Te}_{1.37}$, of size and quality for magnetic and specific-heat measurement, were also obtained from this method in the same tube.

B. Single-crystal x-ray diffraction and magnetic measurements

SCXRD data for $\text{NdSb}_{0.91}\text{Te}_{0.89}$ and $\text{NdSb}_{0.48}\text{Te}_{1.37}$ were collected on a Bruker D8 VENTURE with a PHOTON 3 CPAD detector and a graphite-monochromatized $\text{Mo } K\alpha$ radiation source. Integrated data were corrected with a multiscan absorption correction using SADABS. The structure of $\text{NdSb}_{0.91}\text{Te}_{0.89}$ was solved via SHELXT [27] using intrinsic phasing and refined with SHELXL [28] using the least-squares method, as implemented in the OLEX2 program [29]. Satellite peaks, indicative of a structural modulation, were observed in $\text{NdSb}_{0.48}\text{Te}_{1.37}$. The satellite peaks were indexed to an incommensurate modulation of $q = 0.18b^*$. Refinement was thus carried out using the superspace approach, where the displacive distortion of atomic positions is expressed by a periodic modulation function, yielding a $(3+1)$ -dimensional superspace group. Refinements with the superspace approach were carried out in JANA2006 [30]. This approach included positional, ADP, and site occupancy modulations in the refinement. Determination of Sb/Te occupancy and ordering within the square-net was limited by near-identical scattering power due to their closeness in atomic number ($Z = 51$ and 52 , respectively). At laboratory-accessible x-ray wavelengths, the two species were indistinguishable if present on the same crystallographic site. Thus, for all refinements, atomic occupancies within the Sb/Te square-net were constrained to the stoichiometry derived from EDS.

Magnetic measurements were conducted using the vibrating sample magnetometer (VSM) option of either a Quantum Design DynaCool Physical Property Measurement System (PPMS) or a Magnetic Property Measurement System (MPMS) 3 SQUID magnetometer between 1.8 and 300 K. Single crystals were fixed between quartz paddles in a brass sample holding using GE Varnish, with field applied parallel and perpendicular to the ab plane. Magnetic phase diagrams were generated by collecting temperature-dependent magnetization curves during warming, with varying fields, up to 0.1 T in 0.01 T increments, then up to 5.0 T in 0.1 T increments. Critical temperatures and phase boundaries are derived from peaks in the temperature derivative of the dc magnetic susceptibility, $d\chi/dT$. $d\chi/dT$ curves were plotted to build the magnetic phase diagram in the H - T space.

C. Heat capacity

Heat capacity (C_p) measurements of $\text{NdSb}_{0.48}\text{Te}_{1.37}$ were carried out using a Quantum Design DynaCool PPMS using the semiadiabatic method. The single-crystal sample was fixed to the stage using Apiezon N grease, and measurements were carried out between 1.8 and 300 K. Variable-field

measurements were conducted by applying a magnetic field perpendicular to the ab plane. The crystal-field splitting for a point charge model of Nd^{3+} was computed using PyCrystal-Field [31].

D. Neutron powder diffraction

Neutron powder diffraction data were collected on the WISH instrument at the ISIS Muon and Neutron Source (UK) [32]. The samples were contained in sealed vanadium cans, and the neutron diffraction data were collected in the 1.5–5 K temperature range. The diffraction data were collected in five detector banks each covering 32 degrees of the scattering plane. The Rietveld refinement of the powder data was conducted with the help of the JANA2020 software [30,33]. Group-theoretical calculations and symmetry analysis were performed with the help of the ISOTROPY [34] and ISODISTORT [35] software and of the Bilbao crystallographic server [36–38].

III. RESULTS AND DISCUSSION

A. Crystal structure

The crystal structures of $\text{NdSb}_{0.91}\text{Te}_{0.89}$ and $\text{NdSb}_{0.48}\text{Te}_{1.37}$, as determined by SCXRD at 100 K, are shown in Fig. 1. The structure and lattice parameters of $\text{NdSb}_{0.91}\text{Te}_{0.89}$ are consistent with other reported tetragonal $Ln\text{Sb}_x\text{Te}_{2-x-\delta}$ members, where no CDW ordering is observed. The Sb-Sb bond length within the square net is $3.0574(2)$ Å. The Sb-Sb bond lengths in the square net are significantly longer than what would be expected in a localized and covalent Sb-Sb single bond, as it appears, for example, in elemental Sb (approximately 2.9 Å at 78 K) [39]. The elongated, symmetric bonding can be rationalized by “hypervalent” bonding, where a -1 charge on Sb is stabilized by electron delocalization across the entire net, as detailed by Papoian and Hoffmann [12]. The NdTe layer of the structure displays the aforementioned puckered rocksalt structure, with the Nd-Te bond length nearly parallel to ab (within the unit cell) held constant at $3.1931(2)$ Å, and the bond length parallel to c (across unit cells) held at $3.2788(6)$ Å.

The structure of $\text{NdSb}_{0.48}\text{Te}_{1.37}$ displays a CDW distortion, as evidenced by the appearance of low-intensity satellite peaks visible in the precession images of the diffraction patterns (Fig. S2) [40]. The pattern can be indexed as an incommensurately modulated structure, with a modulation wave vector $q = 0.18b^*$. This modulation wavelength corresponds to an approximate fivefold expansion of the unit cell along b^* . Using the superspace approach to x-ray structure solution and refinement, $\text{NdSb}_{0.48}\text{Te}_{1.37}$ is found to crystallize in the $Pm\bar{m}n (0\beta 0)00 s (3+1)D$ superspace group, and when visualized as a commensurate fivefold approximant, it is isostructural to $\text{CeSb}_{0.51}\text{Te}_{1.40}$ and $\text{GdSb}_{0.46}\text{Te}_{1.48}$, where the (Sb,Te) square net is found to distort into a pattern of zigzag chains and more isolated atoms. This is congruent with our previous studies on the evolving CDWs observed in $\text{GdSb}_x\text{Te}_{2-x-\delta}$ and $\text{CeSb}_x\text{Te}_{2-x-\delta}$. This same structure was found to give rise to an ideal nonsymmorphic Dirac semimetal band structure [15]. We note that our indexing and SCXRD refinement of $\text{NdSb}_{0.48}\text{Te}_{1.37}$ is presented in a nonstandard

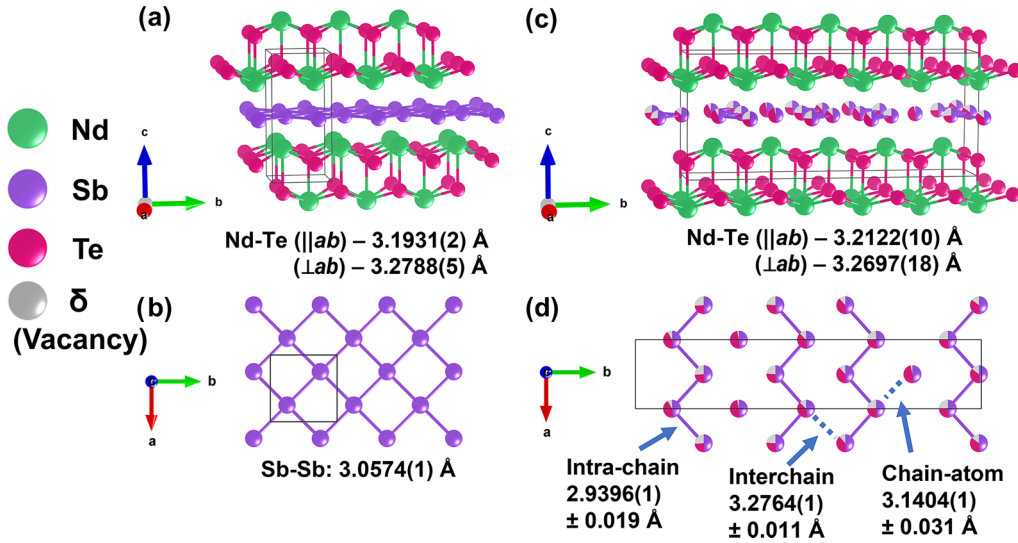


FIG. 1. Crystal structures of (a), (b) $\text{NdSb}_{0.91}\text{Te}_{0.89}$ and (c), (d) $\text{NdSb}_{0.48}\text{Te}_{1.37}$, as determined by single-crystal x-ray diffraction with bond distances given. Bonds in the distorted net of $\text{NdSb}_{0.48}\text{Te}_{1.37}$ are drawn for distances equal to or shorter than the determined Sb-Sb bond length in undistorted $\text{NdSb}_{0.91}\text{Te}_{0.89}$, emphasizing the loss of bond delocalization upon CDW. Bond distances in (d) are shown as their average lengths \pm distance modulation, with errors given in parentheses.

crystallographic setting (c as the long axis instead of b), consistent with previous reporting on $\text{LnSb}_x\text{Te}_{2-x-\delta}$, to describe the distorted square net with the same crystallographic axes as the undistorted parent. Later magnetic refinements are presented in a standard setting in the SI.

Using the Sb-Sb bond length in tetragonal $\text{NdSb}_{0.91}\text{Te}_{0.89}$ as a reference for an undistorted square net with fully delocalized bonding, we discuss the localization and symmetry breaking of the square net in $\text{NdSb}_{0.48}\text{Te}_{1.37}$. The square net breaks into a repeating pattern of parallel chains separated by lines of more isolated (Sb,Te) atoms [Fig. 1(d)]. Intrachain Sb-Sb bonding varies from $2.92105(1)$ to $2.9593(1) \text{ \AA}$, and it remains constant within each chain. The nearest distance from a chain atom to an isolated atom ranges from $3.1098(1)$ to $3.1706(1) \text{ \AA}$. Interchain atom distances are the largest, ranging from $3.2655(1)$ to $3.2872(1) \text{ \AA}$. The significant deviations from the hypervalent bond length found in the undistorted square-net imply a strong localization of bonding along the chain directions, with minimal bonding interactions between the chains. The chain-to-isolated atom distance sits in an intermediate range, larger than the expected value for delocalized bonding, but may carry more bonding interaction than interchain interactions. It is notable that our refinement of $\text{NdSb}_{0.48}\text{Te}_{1.37}$ does not assign site occupancy preference of Sb/Te within the distorted square net. In previous refinements of $\text{GdSb}_{0.45}\text{Te}_{1.53}$, which was carried out with a commensurate supercell, Sb/Te was assigned based on chemical bonding principles, assuming Te to have preference on the isolated atom sites due to its higher valence electron count [21]. The superspace approach allowed the Sb/Te ratio to be fixed, and a site occupancy wave on Te atoms in the net modeled the modulation of electron density due to the CDW and the presence of vacancy. This approach greatly reduces the number of parameters needed to refine the structure and yields a more accurate result with respect to the true and slightly incommensurate periodicity of the structure, as evidenced by quality-of-fit

parameters and minimal residual peak/hole density. We also highlight that isolated atom sites display nearly full total occupancy, implying a greater electron density at these sites. This result adds credence to the tentative assignment of Te at these sites in previous refinements. Regardless of site preference, the substitution of Te into the net is considered to add minimal lattice strain due to its nearly equal radius to Sb. Thus, the CDW distortion is driven by electronic instability that arises from adding additional valence electrons from Te into the square net, breaking the bond delocalization.

The heavy distortion of the square net due to the CDW in $\text{NdSb}_{0.48}\text{Te}_{1.37}$ is contrasted with minimal changes to the bond length within the NdTe layer. The NdTe bond length nearly parallel to ab held constant at $3.2122(1) \text{ \AA}$, and the bond length parallel to c is $3.2699(2) \text{ \AA}$. These bond lengths are quite similar to that in undistorted $\text{NdSb}_{0.91}\text{Te}_{0.89}$, with the deviation well explained by differences in the parent cell lattice parameters between the two. Figure S3a shows the modulation amplitude of bond distances in the NdTe structural unit and within the distorted square net. Nd-Te bonds do not vary more than 0.01 \AA , whereas the amplitude of bond modulations within the distorted square net varies as much as 0.4 \AA . (Fig. S3b) This feature is common to all of the modulated $\text{LnSb}_x\text{Te}_{2-x-\delta}$ we have studied [21,22], and consistent with our understanding of bonding in the square net. We consider the electrons involved in bonding in the NdTe layer to lie well below the Fermi energy, and thus will be unaffected by the CDW. This lack of structural interaction with the CDW will become interesting to consider in our discussion of the magnetic structure and its connection to the CDW.

B. Magnetic measurements and specific heat

In Fig. 2, we present the magnetic phase diagrams of $\text{NdSb}_{0.91}\text{Te}_{0.89}$ [Figs. 2(a) and 2(b)] and $\text{NdSb}_{0.48}\text{Te}_{1.37}$ [Figs. 2(c) and 2(d)], constructed by plotting the first-order

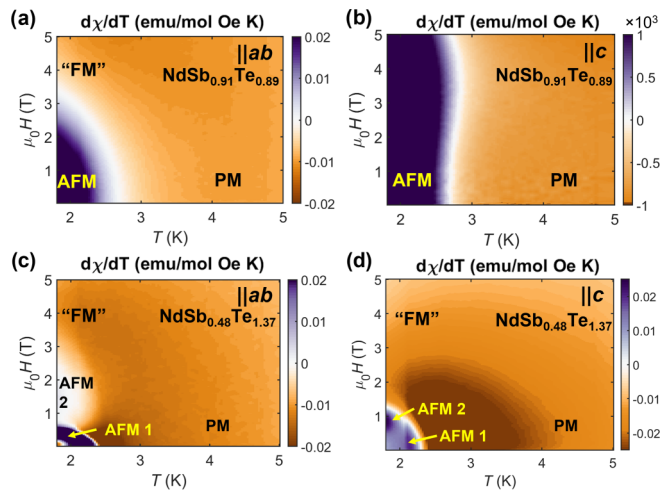


FIG. 2. Magnetic phase diagrams (H vs T) of $\text{NdSb}_{0.91}\text{Te}_{0.89}$ and $\text{NdSb}_{0.48}\text{Te}_{1.37}$. Plots were generated from the first-order derivative of χ over temperature ($d\chi/dT$).

derivative of $\chi(T)$ curves measured along the crystallographic ab plane and c axis. In the case of $\text{NdSb}_{0.91}\text{Te}_{0.89}$, a Néel temperature $T_N = 2.7$ K is observed. A magnetic field of 3 T eventually suppresses the AFM order when applied along the ab plane [Fig. 2(a)]; the system presumably transitions to a fully spin-polarized state at this field (“FM”). If the field is applied along the c axis [Fig. 2(b)], no metamagnetic transition is clearly visible from the variable field moment versus temperature measurements used to construct the phase diagram. Field-dependent magnetization curves show a subtle change in slope at 3 T in the derivative curve (Fig. S4b), and a smaller magnetic moment at all fields compared to in-plane measurements (Fig. S2a). Thus, the feature at 3 T may be an in-plane contribution due to imperfect alignment of the crystal in the applied field. Significantly different moments at the maximum applied field ($M_{7T,ab} \gtrsim 2M_{7T,c}$) along in- and out-of-plane directions further implies magnetic anisotropy (Fig. S4a). These results are similar to previously reported magnetic measurements on tetragonal $\text{NdSb}_x\text{Te}_{2-x-\delta}$, where $x = 0.8$ [25].

In $\text{NdSb}_{0.48}\text{Te}_{1.37}$, the observed T_N is 2.3 K (AFM 1), lower than the tetragonal compound. This contrasts with the behavior observed in Ce and Gd members of $\text{LnSb}_x\text{Te}_{2-x-\delta}$: $\text{CeSb}_x\text{Te}_{2-x-\delta}$ displays an increase in T_N with decreasing x ; $\text{GdSb}_x\text{Te}_{2-x-\delta}$ shows nonlinear behavior where T_N increases to a maximum at $x = 0.48$, and it decreases at lower Sb compositions [22,23]. Measurements with fields applied within the ab plane [Fig. 2(c)] detect a metamagnetic transition at ~ 0.6 T (AFM 2), with a region of enhanced χ that persists to 3 T, where another metamagnetic transition occurs, presumably to a fully spin-polarized state (“FM”). Both phase boundaries are corroborated by magnetization versus field measurements (Fig. S4d) collected at 1.8 K. Measurements with fields applied along the c axis [Fig. 2(d)] indicate a pair of metamagnetic transitions at ~ 0.7 and ~ 1.2 T, which is also observed in the magnetization curves at 1.8 K as a shoulder in the derivative curve followed by a peak with increasing field. The presence of more metamagnetic transitions at lower critical

fields in both directions implies that spins are more readily polarized along either crystallographic direction in comparison to $\text{NdSb}_{0.91}\text{Te}_{0.89}$. Field-dependent magnetization also shows a smaller difference between in- and out-of-plane saturating moments in $\text{NdSb}_{0.48}\text{Te}_{1.37}$ (Fig. S4c), altogether indicating that the CDW phase displays less magnetic anisotropy than its undistorted relative. In addition, the CDW phase exhibits more complex magnetism as compared with the tetragonal one, as evidenced by the multiple metamagnetic transitions.

The magnetic phase diagram of $\text{NdSb}_{0.48}\text{Te}_{1.37}$ can be compared to the isostructural CDW-containing relatives $\text{GdSb}_{0.46}\text{Te}_{1.48}$ and $\text{CeSb}_{0.51}\text{Te}_{1.40}$ [22,23]. $\text{GdSb}_{0.46}\text{Te}_{1.48}$ exhibits a significantly more complex phase diagram than its tetragonal family member $\text{GdSb}_{0.85}\text{Te}_{1.15}$ [21], along all measured directions, but particularly under fields applied along the ab plane, a behavior also observed in $\text{NdSb}_{0.48}\text{Te}_{1.37}$. In the latter case, the magnetic ordering temperature is much lower and so the various magnetic transitions may be more difficult to resolve, whereas the Gd compound shows multiple temperature-induced phase transitions. The observed multiple in-plane transitions contrast with $\text{CeSb}_{0.51}\text{Te}_{1.40}$, where no metamagnetic transitions are observed if a field is applied along ab , but multiple transitions are observed for fields along c . This corresponds with the out-of-plane magnetic structure of its stoichiometric parent, CeSbTe .

To corroborate the observed T_N and field dependence of the magnetic transitions in $\text{NdSb}_{0.48}\text{Te}_{1.37}$, we performed heat capacity measurements on a single crystal (see Fig. 3). At zero applied field, the observed T_N is identical to that observed in the χ plots, and is suppressed with applied field in a manner consistent with them. The spin state of $\text{NdSb}_{0.48}\text{Te}_{1.37}$ can also be determined by integrating the magnetic component of the total heat capacity over temperature ($\frac{C_p}{T}$) to calculate the change in the magnetic entropy (ΔS_{mag}). To determine the magnetic heat capacity, C_{mag} , the phonon contribution to heat capacity was subtracted using a single Debye mode as described in the equation shown below:

$$C_D(\theta_D, T) = 9sR \left(\frac{T}{\theta_D} \right)^3 \int_0^{\frac{\theta_D}{T}} \frac{(\theta/T)^4 e^{\theta/T}}{[e^{\theta/T} - 1]^2} d\frac{\theta}{T}, \quad (1)$$

where s is the oscillator strength, R is the molar Boltzmann constant, and θ_D is the Debye temperature. The parameters extracted from the least-squares fit between $T = 25$ and 265 K are $s = 3.007(8)$ and $\theta_D = 182.8(4)$ K, respectively. The total oscillator strength is in reasonable agreement with the total number of atoms per formula unit in $\text{NdSb}_{0.48}\text{Te}_{1.37}$. In the phonon fit, an Einstein mode was not incorporated because there was no T_{max} in the $\frac{C_p}{T^3}$ plot. Thus, a single Debye mode was sufficient for the phonon fit. The ΔS_{mag} with respect to temperature is found to saturate at $\simeq 4.99$ J/mol K, slightly below what would be expected for an $S = \frac{1}{2}$ spin state ($R \ln 2$). The slight decrease in the ΔS_{mag} results from additional entropy release below $T = 2$ K that is not captured by a linear extrapolation of $C_p/T \rightarrow 0$ at $T = 0$ K. The presence of artifacts and magnetic entropy beyond the phonon subtraction region are viable possibilities; thus the heat capacity analysis had some limitations. Our results notably contrast with entropy observed by Pandey *et al.* in $\text{NdSb}_x\text{Te}_{2-x-\delta}$, where $x = 0.8$, which more closely indicates an $S = \frac{3}{2}$ state

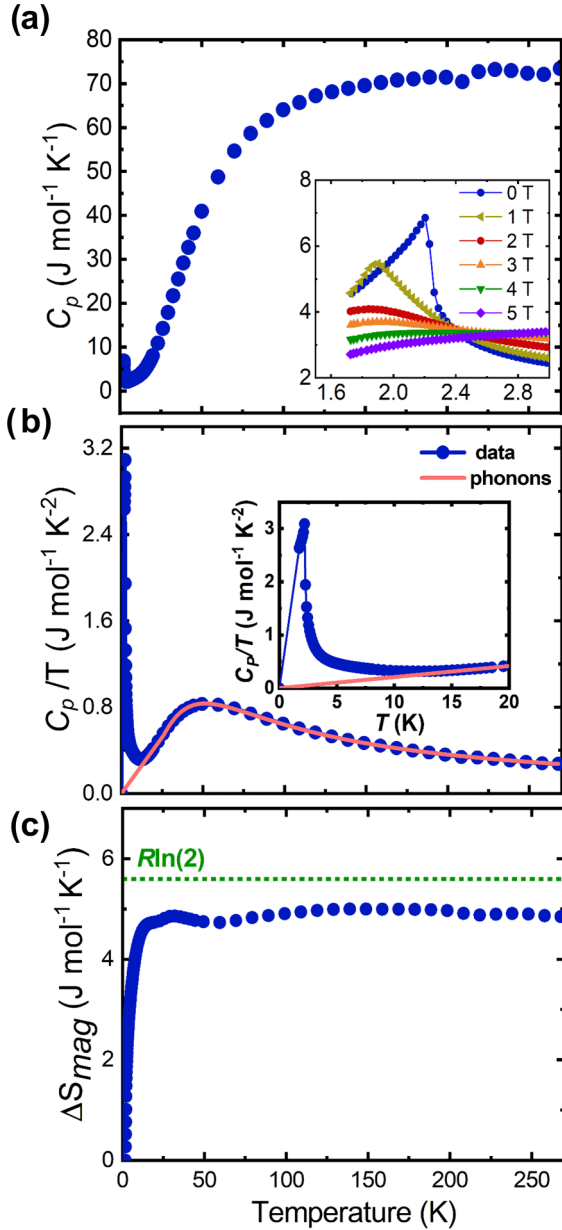


FIG. 3. Heat capacity measurements. (a) Temperature dependence of the heat capacity C_p for NdSb_{0.48}Te_{1.37} at variable applied fields. The inset focuses on low-temperature behavior at applied fields, highlighting the suppression of T_N with applied field. (b) Debye fit of C_p/T with fitted phonon contribution shown. (c) Magnetic entropy S_m calculated from heat capacity data.

consistent with a free Nd³⁺ ion [25]. However, in NdSb_{0.48}Te_{1.37} the computed single-ion crystal field levels are split into doublets (see Fig. S5). The doublets in Nd³⁺ explain the saturation $S = \frac{1}{2}$ spin state in ΔS_{mag} .

C. Neutron diffraction and magnetic structures

The magnetic ground state in zero applied magnetic field for both compounds has been investigated through powder neutron diffraction in the 5–1.5 K temperature range. The paramagnetic data set of NdSb_{0.94}Te_{0.92}, collected at 5 K, is in good agreement with the structural model obtained on

single-crystal specimens [see Fig. S6 and Tables S3 and S4 in the Supplemental Material (SM) for details]. On cooling below $T_N \approx 2$ K, broad magnetic reflections are observed in the diffraction pattern, which indicates a magnetic correlation length significantly shorter than the nuclear one. The peaks can be indexed with the propagation vector $k = (0 \ 1/2 \ 1/2)$. The possible magnetic isotropy subgroups consistent with both the parent structure symmetry and the observed propagation vector were obtained with the help of the ISODISTORT software [35]. The best agreement with the experimental data is obtained for the magnetic space group A_b2_1/c [P_c2_1/c , basis = (0, 1, 1), (−1, 0, 0), (0, −2, 0); origin = (1, 1, 0) in standard settings; see Table S3 in the SM for details]. The refined magnetic structure, together with the magnetic Rietveld plot, are shown in Figs. 4(a) and 4(b). The spin ordering consists of AFM chains that run along the b axis, where the spins lie parallel to b and antiparallel to each other along the chain. A refined moment of $1.674(8)\mu_B$ per Nd was obtained. The two AFM chains within a NdTe layer are shifted by half a unit cell in plane, due to the presence of the n -glide symmetry operation in the parent structure, which leads to one ferromagnetic (J_1) and one antiferromagnetic (J_2) Nd-Nd interaction. This geometrical frustration of the intrachain interactions could be the reason for the very broad magnetic reflections observed in the neutron data. In fact, in VOCl, which is structurally closely related to tetragonal NdSb_{0.94}Te_{0.92}, a lattice distortion, which lifts this frustration, is observed at the magnetic ordering temperature [41]. Since no such distortion is observed NdSb_{0.94}Te_{0.92}, the frustration between the intrachain interaction remains, resulting in the broad magnetic Bragg peaks. In general, the observed magnetic structure is typical for PbFCI-type compounds, as VOCl adopts a very similar one [41]. Still, it is different from that observed in CeSbTe, where spins point along the c axis and the AFM coupling doubles the unit cell [24].

The paramagnetic diffraction pattern of modulated NdSb_{0.48}Te_{1.37}, collected at 5 K, is in agreement with the structural model obtained from the single-crystal data (see Table S7-8 and Fig. S7 in the SM for details). The refinement has been conducted in the $Pmnm(00\gamma)000$ superspace group, and due to the small intensity of the modulation satellite peaks, only the first-order positional modulation parameters have been refined. The obtained structural parameters are reported in the SM, and the refined value of the modulation vector is $q_{CDW} = (0, 0.183(1), 0)$ (with respect to the parent $P4/nmm$ structure). On cooling below $T_N = 2.0(1)$ K, sharp magnetic reflections are observed in the diffraction pattern. These can be indexed with the propagation vector $q_{mag} = (0, -0.408(1), 0)$; the minus sign and the relation with the nuclear modulation vector will be discussed in detail later. The possible magnetic superspace groups consistent with the observed modulation vector and the tetragonal $P4/nmm$ parent structure have been calculated with the help of the ISOTROPY and ISODISTORT software [34,35]. The best agreement with the experimental data has been achieved with the $Pmnm.1'(00\gamma)s00s$ superspace group, and the obtained spin structure and the relative magnetic Rietveld plots are shown in Figs. 4(c) and 4(d) (see Tables S9 and S10 in the SM for detail). The magnetic structure can be refined as an elliptical cycloid with a sinusoidal in plane amplitude

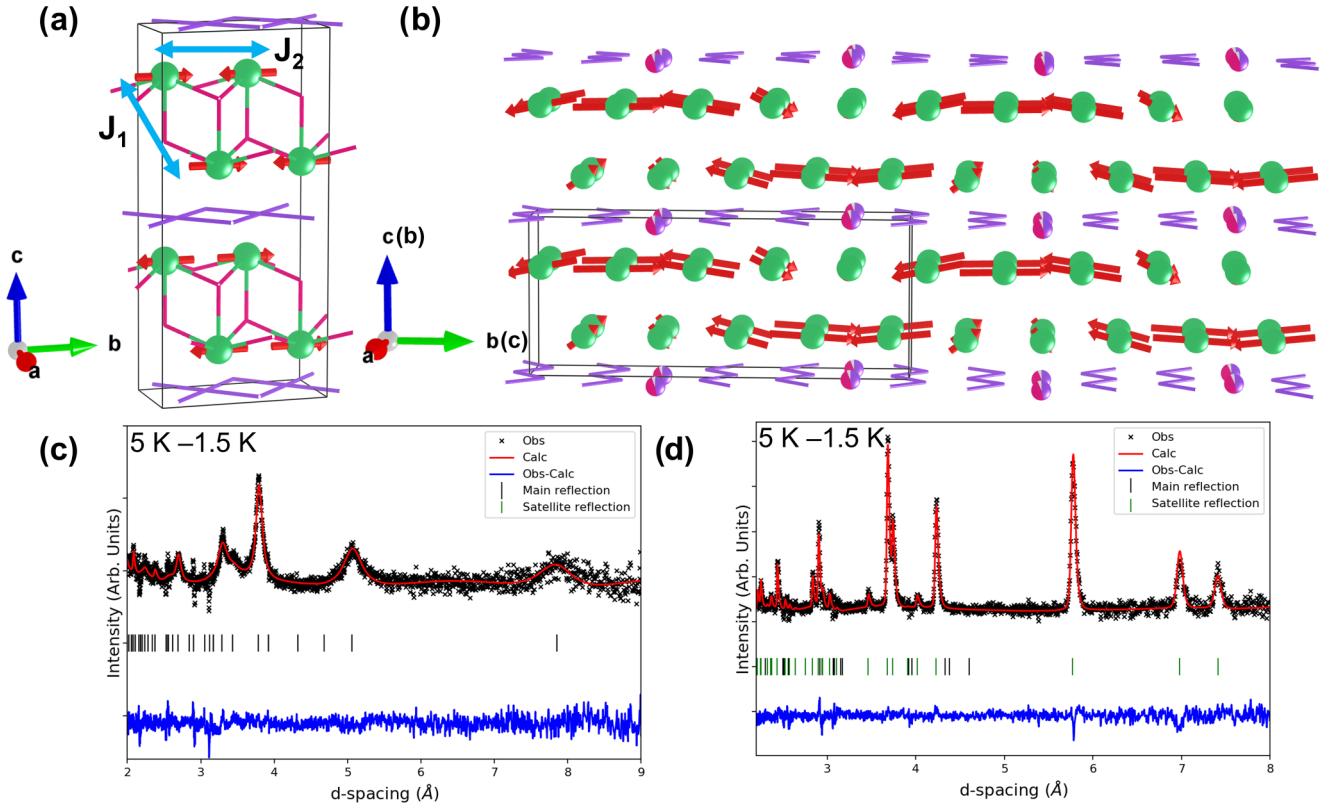


FIG. 4. Magnetic structures determined by neutron diffraction. (a) Magnetic structure of $\text{NdSb}_{0.94}\text{Te}_{0.92}$. (b) Magnetic structure of $\text{NdSb}_{0.48}\text{Te}_{1.37}$, with exchange coupling terms J_1 and J_2 shown. In parentheses, standard crystallographic axes used in Rietveld model are given. (c) Magnetic Rietveld fit for $\text{NdSb}_{0.94}\text{Te}_{0.92}$, with magnetic scattering at 1.5 K plotted by subtraction of nuclear scattering collected at 5 K. (d) Magnetic Rietveld fit for $\text{NdSb}_{0.48}\text{Te}_{1.37}$, with magnetic scattering at 1.5 K plotted by subtraction of nuclear scattering collected at 5 K.

that is ≈ 3 times larger than the out-of-plane cosinusoidal component. The rotation of the moments between adjacent unit cells along the propagation vector is of $\pi - \phi$ (the sign choice of the propagation vector component change the rotation angle from $\pi - \phi$ to $\pi + \phi$). Due to the presence of the $\{n|0000\}$ symmetry element in the superspace group, the two cycloids on the Nd atoms in the NdTe layer are rotating in opposite directions. This suggests that the magnetic interaction between these two positions will average to zero over the period of the magnetic structure. The solution shown in Fig. 4 is the only model that is able to fit the observed intensity correctly; attempts to constrain a constant moment structure with a circular cycloid return worse fits of the data, as shown in Fig. S8. The same is true for attempts using a positive propagation vector, i.e., a cycloid with a rotation angle of $\pi + \phi$ (Fig. S9).

D. Coupling between the CDW and the elliptical cycloid

It is worth underlining the strong coupling between the observed elliptical magnetic structure and the charge density wave, which occurs above the magnetic transition. By observing the value of the modulation vectors, one can notice that they are related by $1 + 2\nu_2 = \nu_1$, where ν_1 and ν_2 are the components of the CDW and cycloidal modulation vectors, respectively. Indeed, this relation can be rewritten, in vectorial form, as $q_{\text{CDW}} + 2q_{\text{mag}} = (0\bar{1}0)$, which suggests that the

nuclear modulation can be considered the second harmonic of the magnetic distortion, with the caveat that with respect to the parent $P4/nmm$ structure the two propagation vectors have opposite sign (the sign choice being a consequence of symmetry decomposition from the parent structure).

With respect to the parent $P4/nmm$ structure, the nuclear modulation transforms as the Δ_3 irreducible representation with the order parameter $(\delta, \delta^*, \eta, \eta^*)$, defined in a complex basis, and modulation vector $q_{\text{CDW}} = (0, \nu_1, 0)$. On the other hand, the elliptical magnetic structure transforms as the time-even irreducible representation $m\Delta_2$ with the order parameter (μ, μ^*, ξ, ξ^*) and propagation vector $q_{\text{CDW}} = (0, \nu_2, 0)$. By inspecting the transformation matrices of the generators of the $P4/nmm.1'$ space group for these two irreducible representations (reported in Table S9), it is possible to write a third-degree free energy invariant that couples these two distortions. The coupling term is $\delta^* \mu^2 + \delta \mu^{*2} + \eta^* \xi^2 + \eta \xi^{*2}$ and it is allowed only if the components of the propagation vector of the two distortions verify the condition $1 + 2\nu_2 = \nu_1$. This coupling term gives a natural explanation why the system decides to order magnetically with the observed propagation vector and the observed symmetry. In fact, by choosing the $m\Delta_2$ symmetry for the magnetic order parameter and the value of the magnetic propagation vector such that $1 + 2\nu_2 = \nu_1$, the system lowers its free energy by coupling to the nuclear modulation already present above the magnetic transition. The coupling term also provides the system a mechanism to

relieve the magnetic frustration as can be appreciated from the sharper magnetic peaks in $\text{NdSb}_{0.48}\text{Te}_{1.37}$ compared to $\text{NdSb}_{0.94}\text{Te}_{0.92}$. The coupling term alone does not justify the elliptical character of the cycloidal structure, which is likely the result of the competition between the magnetic anisotropy observed in the magnetization data and the magnetoelastic coupling term with the CDW. The energy gain offered by activating the coupling term could resolve the frustration of the Nd-Nd interactions by stabilizing the elliptical cycloid structure instead of the collinear structure observed in tetragonal $\text{NdSb}_{0.94}\text{Te}_{0.92}$.

To further confirm the coupling term, the diffraction data collected at 1.5 K were refined in the $Pmnm.1'(00\gamma)_{s00s}$ magnetic superspace group, refining the magnetic modulation as first-order harmonics and the nuclear modulation as second-order harmonics. The results of the refinement are summarized in Tables S9 and S10 and the corresponding Rietveld plots are shown in Fig. S10. As can be appreciated, the refined nuclear modulation is in good agreement with the refined structure at 5 K, as well as the single-crystal data.

E. Discussion

Both charge- and spin-density waves are phenomena driven by Fermi surface nesting, and are frequently considered as competing phase transitions, as they both result in the opening of an energy gap to relieve the electronic instability of the nesting [13]. The coexistence of both in a system implies the coupling of charge and spin degrees of freedom, which has been observed in metallic Cr [42,43], FeTe_{1-y} [44], and in layered nickelate $\text{La}_4\text{Ni}_3\text{O}_{10}$ [45], and recently, KMn_6Bi_5 [46]. In a majority of these cases, CDW and SDW onset coincide at the same transition temperature, frequently attributed to magnetoelastic coupling, and the CDW can be considered as a secondary order parameter induced by the SDW [47]. In $\text{NdSb}_{0.48}\text{Te}_{1.37}$, the CDW is observed at room temperature, well above the appearance of the spin modulation. In this case, RKKY interactions influence the spin modulation as the density of states is dominated by conduction electrons from the distorted (Sb,Te) square net, which mediate the ordering of localized Nd moments while carrying the information of the lattice modulation to the spins. Thus, the CDW plays a role in “templating” the resulting spin wave below T_N , as well as relieving the magnetic frustration apparent by comparison to $\text{NdSb}_{0.94}\text{Te}_{0.92}$. A similar “templating” effect has been observed in $\text{CaMn}_7\text{O}_{12}$ [48] in which the observed orbital density wave [49] influence the exchange interactions stabilizing the intermediate temperature SDW [48], and in $\zeta\text{-Mn}_2\text{O}_3$, where the commensurate orbital order drives the selection of the magnetic ground state [50]. The “templating” effect of the CDW and the subsequent relief of the exchange frustration explains why the temperature-induced antiferromagnetic transitions occur more sharply in $\text{NdSb}_{0.48}\text{Te}_{1.37}$. The lower critical field for metamagnetic transitions, both in-plane (ab) and in the out-of-plane direction (c), agree well with the magnetic structure, since the elliptical cycloid lies in the bc plane.

The coupling term constructed for $\text{NdSb}_{0.48}\text{Te}_{1.37}$ also implies that for a CDW phase involving two arms of the star of \mathbf{q} , the resultant magnetic structures will have the same

number of arms involved. Given that multi- \mathbf{q} magnetic states are known to give rise to skyrmion phases and other related spin textures, it is possible that CDW can be used as a tool to access them via RKKY interactions in addition to the more-common Dzyaloshinskii-Moriya interaction, which drives their presence in other systems. Indeed, it has been shown that densely packed skyrmion lattices can exist in centrosymmetric crystals, where the skyrmions are believed to originate from frustrated RKKY interactions [51–54]. Recent powder neutron diffraction on stoichiometric HoSbTe and TbSbTe , tetragonal members of $\text{LnSb}_x\text{Te}_{2-x-\delta}$, reveal complex, multi- \mathbf{q} magnetic structures, requiring multiple commensurate propagation vectors in the ground state, which transform to incommensurate upon warming while still below T_N [55]. Exploring the synthesis of their CDW-containing derivatives may hold potential to access such skyrmion lattices. In previously mentioned $\text{GdSb}_{0.46}\text{Te}_{1.48}$, a low-field region of the magnetic phase diagram in the out-of-plane direction shows possible signatures of an antiferromagnetic skyrmion phase by magneto-entropic analysis. The multiple low-field transitions present in the out-of-plane magnetization of $\text{NdSb}_{0.48}\text{Te}_{1.37}$ may bear relation to the magnetic phases observed in $\text{GdSb}_{0.46}\text{Te}_{1.48}$, also hinting to the role that the CDW may play therein. A recent single-crystal neutron diffraction study on single- q , near-sixfold CDW phase $\text{GdSb}_{0.71}\text{Te}_{1.22}$ reports the appearance of two magnetic phases, which arise subsequently below T_N and below the final transition at 5 K, respectively [56]. The multi- \mathbf{q} CDW phase $\text{CeSb}_{0.10}\text{Te}_{1.79}$ shows complex out-of-plane metamagnetic transitions in the form of a “devil’s staircase” [22] in the out-of-plane magnetization, where it is also suggested that the CDW couples to a type of spin wave. However, in this system, the CDW wave vectors contain out-of-plane components, which may allow interaction with the expected out-of-plane spin structure.

IV. CONCLUSION

In conclusion, we have investigated the crystal structure, magnetic properties, and magnetic structure of the undistorted square-net TSM $\text{NdSb}_{0.94}\text{Te}_{0.92}$ and its CDW-distorted relative $\text{NdSb}_{0.48}\text{Te}_{1.37}$ to understand the interactions between the charge density wave and magnetism in $\text{LnSb}_x\text{Te}_{2-x-\delta}$ systems. $\text{NdSb}_{0.94}\text{Te}_{0.92}$ is isostructural to other stoichiometric LnSbTe , where delocalized bonding stabilizes the Sb square net. $\text{NdSb}_{0.48}\text{Te}_{1.37}$ exhibits a CDW distortion that breaks the square net into zigzag chains with isolated atoms, isostructural to other $\text{LnSb}_x\text{Te}_{2-x-\delta}$ with similar x and nearly commensurate ($\mathbf{q} = 0.18\mathbf{b}^*$). While $\text{NdSb}_{0.94}\text{Te}_{0.92}$ behaves as a typical collinear antiferromagnet with a T_N of 2.7 K, $\text{NdSb}_{0.48}\text{Te}_{1.37}$ displays additional complex magnetism, with a lower T_N of 2.3 K and additional metamagnetic transitions. $\text{NdSb}_{0.48}\text{Te}_{1.37}$ has an elliptical cycloid magnetic structure with a propagation vector $\mathbf{q} = -0.41\mathbf{b}^*$. The near-integer multiple of the CDW vector provides a rare example of CDW inducing complex spin order through coupling of propagation vectors, as well as the most direct evidence of CDW coupling with magnetism in $\text{LnSb}_x\text{Te}_{2-x-\delta}$ to date. This is also an example of a magnetic structure of a CDW phase within the $\text{LnSb}_x\text{Te}_{2-x-\delta}$ family. The existence of the CDW above the magnetic transition

temperature suggests that it plays a role in “templating” the spin interactions between Ln atoms via RKKY interaction. Furthermore, the complexity of the magnetism and the richness of CDW phases accessible in $LnSb_xTe_{2-x-\delta}$ phases suggest that it is possible to achieve RKKY interaction-induced skyrmions in these materials.

ACKNOWLEDGMENTS

This work is supported by an NSF CAREER grant (DMR-2144295) to L.M.S. Additional support was provided by the Air Force Office of Scientific Research under Award No. FA9550-20-1-0246. This work was further supported by

the Gordon and Betty Moore Foundation (EPiQS Synthesis Award) through Grant No. GBMF9064, the David and Lucille Packard Foundation, the Alfred P. Sloan Foundation, and the Arnold and Mabel Beckman Foundation through a BYI grant awarded to L.M.S. and an AOB postdoctoral fellowship awarded to J.F.K. T.B. acknowledges support from NSF-MRSEC through the Princeton Center for Complex Materials NSF-DMR-2011750. T.H.S. is grateful to Marceline Martineau for helpful discussions. F.O. and P.M. are grateful to Dr. Dmitry Khalyavin for the very fruitful discussion. For the purpose of open access, the author has applied a creative commons attribution (C.C., B.Y.) licence to any author-accepted manuscript version arising.

-
- [1] S. Klemenz, S. Lei, and L. M. Schoop, Topological semimetals in square-net materials, *Annu. Rev. Mater. Res.* **49**, 185 (2019).
- [2] S. Klemenz, A. K. Hay, S. M. Teicher, A. Topp, J. Cano, and L. M. Schoop, The role of delocalized chemical bonding in square-net-based topological semimetals, *J. Am. Chem. Soc.* **142**, 6350 (2020).
- [3] S. Klemenz, L. Schoop, and J. Cano, Systematic study of stacked square nets: From dirac fermions to material realizations, *Phys. Rev. B* **101**, 165121 (2020).
- [4] L. M. Schoop, F. Pielhofer, and B. V. Lotsch, Chemical principles of topological semimetals, *Chem. Mater.* **30**, 3155 (2018).
- [5] J. Liu, J. Hu, H. Cao, Y. Zhu, A. Chuang, D. Graf, D. J. Adams, S. M. A. Radmanesh, L. Spinu, I. Chiorescu, and Z. Mao, Nearly massless Dirac fermions hosted by Sb square net in $BaMnSb_2$, *Sci. Rep.* **6**, 30525 (2016).
- [6] J. Park, G. Lee, F. Wolff-Fabris, Y. Y. Koh, M. J. Eom, Y. K. Kim, M. A. Farhan, Y. J. Jo, C. Kim, J. H. Shim, and J. S. Kim, Anisotropic Dirac Fermions in a Bi Square Net of $SrMnBi_2$, *Phys. Rev. Lett.* **107**, 126402 (2011).
- [7] J. Hu, Z. Tang, J. Liu, X. Liu, Y. Zhu, D. Graf, K. Myhro, S. Tran, C. N. Lau, J. Wei, and Z. Mao, Evidence of Topological Nodal-Line Fermions in $ZrSiSe$ and $ZrSiTe$, *Phys. Rev. Lett.* **117**, 016602 (2016).
- [8] H. Wu, A. M. Hallas, X. Cai, J. Huang, J. S. Oh, V. Loganathan, A. Weiland, G. T. McCandless, J. Y. Chan, S.-K. Mo, D. Lu, M. Hashimoto, J. Denlinger, R. J. Birgeneau, A. H. Nevidomskyy, G. Li, E. Morosan, and M. Yi, Nonsymmorphic symmetry-protected band crossings in a square-net metal $PtPb_4$, *npj Quantum Mater.* **7**, 31 (2022).
- [9] K. Wang, D. Graf, L. Wang, H. Lei, S. W. Tozer, and C. Petrovic, Two-dimensional dirac fermions and quantum magnetoresistance in $CaMnBi_2$, *Phys. Rev. B* **85**, 041101(R) (2012).
- [10] S. Borisenko, D. Evtushinsky, Q. Gibson, A. Yaresko, K. Koepernik, T. Kim, M. Ali, J. van den Brink, M. Hoesch, A. Fedorov, E. Haubold, Y. Kushnirenko, I. Soldatov, R. Schäfer, and R. J. Cava, Time-reversal symmetry breaking type-II Weyl state in $YbMnBi_2$, *Nat. Commun.* **10**, 3424 (2019).
- [11] L. M. Schoop, M. N. Ali, C. Straßer, A. Topp, A. Varykhalov, D. Marchenko, V. Duppel, S. S. P. Parkin, B. V. Lotsch, and C. R. Ast, Dirac cone protected by non-symmorphic symmetry and three-dimensional dirac line node in $zrsi$, *Nat. Commun.* **7**, 11696 (2016).
- [12] G. A. Papoian and R. Hoffmann, Hypervalent bonding in one, two, and three dimensions: Extending the zintl-klemm concept to nonclassical electron-rich networks, *Angew. Chem. Int. Ed.* **39**, 2408 (2000).
- [13] G. Grüner, Density waves in solids, in *Frontiers in Physics*, Advanced Book Vol. 89 (Addison-Wesley, Reading, MA, 1994).
- [14] M. D. Johannes and I. I. Mazin, Fermi surface nesting and the origin of charge density waves in metals, *Phys. Rev. B* **77**, 165135 (2008).
- [15] S. Lei, S. M. Teicher, A. Topp, K. Cai, J. Lin, G. Cheng, T. H. Salters, F. Rodolakis, J. L. McChesney, S. Lapidus, N. Yao, D. Marchenko, A. Varykhalov, C. R. Ast, R. Car, J. Cano, M. G. Vergniory, N. P. Ong, and L. M. Schoop, Band engineering of dirac semimetals using charge density waves, *Adv. Mater.* **33**, 2101591 (2021).
- [16] A. Zunger, Beware of plausible predictions of fantasy materials, *Nature* **566**, 447 (2019).
- [17] B. Bradlyn, L. Elcoro, J. Cano, M. G. Vergniory, Z. Wang, C. Felser, M. I. Aroyo, and B. A. Bernevig, Topological quantum chemistry, *Nature (London)* **547**, 298 (2017).
- [18] A. Weiland, D. G. Chaparro, M. G. Vergniory, E. Derunova, J. Yoon, I. W. H. Oswald, G. T. McCandless, M. Ali, and J. Y. Chan, Band structure engineering of chemically tunable $LnSbTe$ ($Ln = La, Ce, Pr$), *APL Mater.* **7**, 101113 (2019).
- [19] M. G. Vergniory, L. Elcoro, C. Felser, N. Regnault, B. A. Bernevig, and Z. Wang, A complete catalogue of high-quality topological materials, *Nature (London)* **566**, 480 (2019).
- [20] E. DiMasi, B. Foran, M. C. Aronson, and S. Lee, Stability of charge-density waves under continuous variation of band filling in $LaTe_{2-x}Sb_x$ ($0 \leq x \leq 1$), *Phys. Rev. B* **54**, 13587 (1996).
- [21] S. Lei, V. Duppel, J. M. Lippmann, J. Nuss, B. V. Lotsch, and L. M. Schoop, Charge density waves and magnetism in topological semimetal candidates $GdSb_xTe_{2-x-\delta}$, *Adv. Quantum Technol.* **2**, 1900045 (2019).
- [22] R. Singha, T. H. Salters, S. M. Teicher, S. Lei, J. F. Khoury, N. P. Ong, and L. M. Schoop, Evolving devil’s staircase magnetization from tunable charge density waves in nonsymmorphic dirac semimetals, *Adv. Mater.* **33**, 2103476 (2021).
- [23] S. Lei, A. Saltzman, and L. M. Schoop, Complex magnetic phases enriched by charge density waves in the topological semimetals $GdSb_xTe_{2-x-\delta}$, *Phys. Rev. B* **103**, 134418 (2021).

- [24] L. M. Schoop, A. Topp, J. Lippmann, F. Orlandi, L. MÜchler, M. G. Vergniory, Y. Sun, A. W. Rost, V. DuppeL, M. Krivenkov, S. Sheoran, P. Manuel, A. Varykhalov, B. Yan, R. K. Kremer, C. R. Ast, and B. V. Lotsch, Tunable weyl and dirac states in the nonsymmorphic compound cesbte, *Sci. Adv.* **4**, eaar2317 (2018).
- [25] K. Pandey, R. Basnet, A. Wegner, G. Acharya, M. R. U. Nabi, J. Liu, J. Wang, Y. K. Takahashi, B. Da, and J. Hu, Electronic and magnetic properties of the topological semimetal candidate NdSbTe, *Phys. Rev. B* **101**, 235161 (2020).
- [26] V. F. Sears, Neutron scattering lengths and cross sections, *Neutron News* **3**, 26 (1992).
- [27] G. M. Sheldrick, Shelxt-integrated space-group and crystal-structure determination, *Acta Cryst. A* **71**, 3 (2015).
- [28] G. M. Sheldrick, A short history of SHELX, *Acta Cryst. A* **64**, 112 (2008).
- [29] O. V. Dolomanov, L. J. Bourhis, R. J. Gildea, J. A. K. Howard, and H. Puschmann, OLEX2: A complete structure solution, refinement and analysis program, *J. Appl. Cryst.* **42**, 339 (2009).
- [30] V. Petříček, M. Dušek, and L. Palatinus, Crystallographic computing system JANA2006: General features, *Z. Kristallogr.* **229**, 345 (2014).
- [31] A. Scheie, PyCrystalField: Software for calculation, analysis and fitting of crystal electric field Hamiltonians, *J. Appl. Cryst.* **54**, 356 (2021).
- [32] L. C. Chapon, P. Manuel, P. G. Radaelli, C. Benson, L. Perrott, S. Ansell, N. J. Rhodes, D. Raspino, D. Duxbury, E. Spill, and J. Norris, Wish: The new powder and single crystal magnetic diffractometer on the second target station, *Neutron News* **22**, 22 (2011).
- [33] V. Petříček, M. Henriques, and M. Dušek, JANA2020—magnetic option, *Acta Cryst. A* **77**, C175 (2021).
- [34] H. T. Stokes, D. M. Hatch, and B. J. Campbell, ISOTROPY Software Suite, iso.byu.edu
- [35] B. J. Campbell, H. T. Stokes, D. E. Tanner, and D. M. Hatch, ISODISPLACE: A web-based tool for exploring structural distortions, *J. Appl. Cryst.* **39**, 607 (2006).
- [36] M. I. Aroyo, A. Kirov, C. Capillas, J. M. Perez-Mato, and H. Wondratschek, Bilbao Crystallographic Server. II. Representations of crystallographic point groups and space groups, *Acta Cryst. A* **62**, 115 (2006).
- [37] M. I. Aroyo, J. M. Perez-Mato, C. Capillas, E. Kroumova, S. Ivantchev, G. Madariaga, A. Kirov, and H. Wondratschek, Bilbao crystallographic server: I. databases and crystallographic computing programs, *Z. Kristallogr.* **221**, 15 (2006).
- [38] L. Elcoro, B. Bradlyn, Z. Wang, M. G. Vergniory, J. Cano, C. Felser, B. A. Bernevig, D. Orobengoa, G. de la Flor, and M. I. Aroyo, Double crystallographic groups and their representations on the Bilbao Crystallographic Server, *J. Appl. Cryst.* **50**, 1457 (2017).
- [39] C. S. Barrett, P. Cucka, and K. Haefner, The crystal structure of antimony at 4.2, 78 and 298 °K, *Acta Cryst.* **16**, 451 (1963).
- [40] See Supplemental Material at <http://link.aps.org/supplemental/10.1103/PhysRevMaterials.7.044203> for SCXRD precession images, additional magnetic data, Rietveld refinements, crystallographic data tables from SCXRD and Rietveld refinements, and group-theoretical tables.
- [41] A. C. Komarek, T. Taetz, M. T. Fernández-Díaz, D. M. Trots, A. Möller, and M. Braden, Strong magnetoelastic coupling in VOCl: Neutron and synchrotron powder x-ray diffraction study, *Phys. Rev. B* **79**, 104425 (2009).
- [42] E. Fawcett, Spin-density-wave antiferromagnetism in chromium, *Rev. Mod. Phys.* **60**, 209 (1988).
- [43] Y. Hu, T. Zhang, D. Zhao, C. Chen, S. Ding, W. Yang, X. Wang, C. Li, H. Wang, D. Feng, and T. Zhang, Real-space observation of incommensurate spin density wave and coexisting charge density wave on Cr (001) surface, *Nat. Commun.* **13**, 445 (2022).
- [44] M. Enayat, Z. Sun, U. R. Singh, R. Aluru, S. Schmaus, A. Yaresko, Y. Liu, C. Lin, V. Tsurkan, A. Loidl, J. Deisenhofer, and P. Wahl, Real-space imaging of the atomic-scale magnetic structure of Fe_{1+y}Te, *Science* **345**, 653 (2014).
- [45] J. Zhang, D. Phelan, A. S. Botana, Y.-S. Chen, H. Zheng, M. Krogstad, S. G. Wang, Y. Qiu, J. A. Rodriguez-Rivera, R. Osborn, S. Rosenkranz, M. R. Norman, and J. F. Mitchell, Intertwined density waves in a metallic nickelate, *Nat. Commun.* **11**, 6003 (2020).
- [46] J.-K. Bao, H. Cao, M. J. Krogstad, K. M. Taddei, C. Shi, S. Cao, S. H. Lapidus, S. van Smaalen, D. Y. Chung, M. G. Kanatzidis, S. Rosenkranz, and O. Chmaissem, Spin and charge density waves in the quasi-one-dimensional KMn₆Bi₅, *Phys. Rev. B* **106**, L201111 (2022).
- [47] J. C. Tolédano and P. Tolédano, *The Landau Theory of Phase Transitions: Application to Structural, Incommensurate, Magnetic, and Liquid Crystal Systems*, World Scientific Lecture Notes in Physics (World Scientific, Singapore, 1987), Vol. 3.
- [48] R. D. Johnson, D. D. Khalyavin, P. Manuel, A. Bombardi, C. Martin, L. C. Chapon, and P. G. Radaelli, Modulated spin helicity stabilized by incommensurate orbital density waves in a quadruple perovskite manganite, *Phys. Rev. B* **93**, 180403(R) (2016).
- [49] N. Perks, R. Johnson, C. Martin, A. Bombardi, C. Martin, L. Chapon, and P. G. Radaelli, Magneto-orbital helices as a route to coupling magnetism and ferroelectricity in multiferroic *camn7O12*, *Nat. Commun.* **3**, 1277 (2012).
- [50] D. D. Khalyavin, R. D. Johnson, P. Manuel, A. A. Tsirlin, A. M. Abakumov, D. P. Kozlenko, Y. Sun, L. Dubrovinsky, and S. V. Ovsyannikov, Magneto-orbital texture in the perovskite modification of MN₂O₃, *Phys. Rev. B* **98**, 014426 (2018).
- [51] R. Takagi, N. Matsuyama, V. Ukleev, L. Yu, J. S. White, S. Francoual, J. R. L. Mardegan, S. Hayami, H. Saito, K. Kaneko, K. Ohishi, Y. Ōnuki, T.-H. Arima, Y. Tokura, T. Nakajima, and S. Seki, Square and rhombic lattices of magnetic skyrmions in a centrosymmetric binary compound, *Nat. Commun.* **13**, 1472 (2022).
- [52] M. Hirschberger, T. Nakajima, S. Gao, L. Peng, A. Kikkawa, T. Kurumaji, M. Kriener, Y. Yamasaki, H. Sagayama, H. Nakao, K. Ohishi, K. Kakurai, Y. Taguchi, X. Yu, T.-H. Arima, and Y. Tokura, Skyrmion phase and competing magnetic orders on a breathing kagomé lattice, *Nat. Commun.* **10**, 5831 (2019).
- [53] N. D. Khanh, T. Nakajima, X. Yu, S. Gao, K. Shibata, M. Hirschberger, Y. Yamasaki, H. Sagayama, H. Nakao, L. Peng, K. Nakajima, R. Takagi, T.-H. Arima, Y. Tokura, and S. Seki, Nanometric square skyrmion lattice in a centrosymmetric tetragonal magnet, *Nat. Nanotechnol.* **15**, 444 (2020).
- [54] T. Kurumaji, T. Nakajima, M. Hirschberger, A. Kikkawa, Y. Yamasaki, H. Sagayama, H. Nakao, Y. Taguchi, T.-H. Arima, and Y. Tokura, Skyrmion lattice with a giant topological Hall

- effect in a frustrated triangular-lattice magnet, [Science](#) **365**, 914 (2019).
- [55] I. Plokhikh, V. Pomjakushin, D. J. Gawryluk, O. Zaharko, and E. Pomjakushina, Competing magnetic phases in $LnSbTe$ ($Ln = Ho$ and Tb), [Inorg. Chem.](#) **61**, 11399 (2022).
- [56] I. Plokhikh, O. Fabelo, L. Prodan, M. Wörle, E. Pomjakushina, A. Cervellino, V. Tsurkan, I. Kézsmárki, and O. Zaharko, Magnetic and crystal structure of the antiferromagnetic skyrmion candidate $GdSb_{0.71}Te_{1.22}$, [J. Alloys Compd.](#) **936**, 168348 (2023).